Acta Materialia 206 (2021) 116596

Contents lists available at ScienceDirect

Acta Materialia

journal homepage: www.elsevier.com/locate/actamat

Effect of external electric field on diffusivity and flash sintering of 8YSZ: A molecular dynamics study

Wenwu Xu[a,*], Andrey Maksymenko[a], Shahrier Hasan[a], Juan J. Meléndez[b,c], Eugene Olevsky[a,*]

[a] Department of Mechanical Engineering, San Diego State University, San Diego, CA 92182, USA
[b] Department of Physics, Universidad de Extremadura, Av. de Elvas, s/n, 06006 Badajoz, Spain
[c] Institute of Advanced Scientific Computing of Extremadura, Av. de Elvas, s/n, 06006 Badajoz, Spain

ARTICLE INFO

Article history:
Received 28 September 2020
Revised 12 December 2020
Accepted 18 December 2020
Available online 23 December 2020

Keywords:
Flash Sintering
Molecular dynamics
Non-thermal (E-field) mechanism
Diffusion
Defects
8YSZ system

ABSTRACT

The atomistic structural modification and ionic diffusivity in 8YSZ at elevated temperature with the presence of an external electric field (E-field) were investigated by molecular dynamics (MD) simulations. As an example, a sufficiently large system of atomic configuration for a bi-crystal $\sum 5(310)/[001]$ grain boundary (GB) model was studied. MD results show that the E-field promotes the formation of Frenkel pair defects. Notably, some Zr ions diffuse out of GB regions at E-field$\gtrsim$500-1000V/cm, resulting in an "avalanche" of cation vacancies at GBs and reduction of GB space charge. Consequently, the diffusivities of cations and anions are enhanced in the 8YSZ system with the presence of E-field. The atomistic level understanding of E-field induced structural modifications and ionic diffusivities provide an in-depth insight to unravel the flash sintering mechanisms of ionic ceramics, especially the coupled thermal-field effect during the flash sintering process.

1. Introduction

The structural evolution and mechanisms of sintering process of ceramic powders by electric current assisted sintering (ECAS) technique have been widely studied over the past few decades [1–12]. A number of influential works and reviews have been written recently on the ECAS techniques and applications, such as [13] by R. Castro, [7] by J. Garay, [14] by O. Graeve, [3] by O. Guillon, [15] by K. Lu, [8,16] by J. Luo, [4,17] by Z. Munir, [12] by R. Orrù, [18] by X. Song, and so on. There has been a continuous debate going on whether the external electric field (E-field) provides additional mechanisms to the sintering process, in addition to the thermal runaway Joule heating. This debate became more heated after a significant experiment has been performed by Cologna, Rashkova and Raj [19]. In the experiment, the yttrium-stabilized zirconia (YSZ) was fully sintered within 5 seconds when the strength of the E-field is sufficiently high (e.g., $\gtrsim$60V/cm) at certain temperatures. This is called "flash sintering (FS)" due to its extremely short sintering time compared to traditional sintering techniques, which usually require hours or even longer.

Previously developed ECAS techniques, such as spark plasma sintering (SPS) applied with a much lower strength of E-field (e.g., $\lesssim$10-20V/cm), were also used to sinter YSZ powders. The SPS sintering time of YSZ is of the order of minutes, which is also significantly longer than that of the FS process [20,21]. Clearly, there is an ultra-rapid ("flash") event happening during the FS process when the E-field is greater than a certain threshold value. While thermal runaway Joule heating mechanism contributes significantly to the rapid sintering process, it alone cannot fully explain the observed "flash" shrinkage rate of the material [1,8,22–24]. In other words, the ultra-rapid sintering process cannot be explained by the enhancement of a single mass transport mechanism resulting from the temperature rise alone.

A great number of efforts, both experimentally and theoretically, have been carried out to explore the mechanisms of FS process [8,25–34], but lack of fundamental and quantitative descriptions at the atomic level. Atomistic insights can clarify various sintering mechanisms proposed in the literature because sintering of crystalline materials is essentially originated and achieved by the atomic level diffusional activities. Particularly in the sintering of ionic ceramics, the accurate description of atomistic diffusivities of

* Corresponding authors.
E-mail addresses: wenwu.xu@sdsu.edu (W. Xu), eolevsky@sdsu.edu (E. Olevsky).

https://doi.org/10.1016/j.actamat.2020.116596

ions and/or vacancies as a function of E-field is a key to uncover the fundamental understanding of flash sintering mechanisms and other ECAS techniques.

As one of the most realizable yet efficient modeling approaches for studying atomistic structure and dynamics, molecular dynamics (MD) simulations have become a preferred method to study the structural modifications and diffusivity as a function of temperature at the atomic scale [35–43]. For example, MD simulations have been used to compute the diffusivity of both cations and anions in a variety of YSZ systems [37,44–46]. These MD simulations predict atomistic structures of YSZ and diffusion coefficients of various ions in agreement with relevant experiments and ab initio quantum mechanical calculations. In this work, using the 8YSZ (8mol% Y_2O_3-doped ZrO_2) as an example, we will perform MD simulations for a bi-crystal model at elevated temperatures (T) and with the presence of E-field. From the MD modeling, we will investigate the atomic structure of 8YSZ and quantify the diffusion coefficients of Y, Zr and O ions as a function of T and E-field. Based on MD results, we will discuss the contribution of non-thermal mechanism of the E-field during the flash sintering process from the atomistic point of view.

2. Methodology

2.1. Bi-crystal model creation

The common practice of creating a bi-crystal model of YSZ is to, first of all, create a bi-crystal model of ZrO_2. Then, depending on the concentration of Y_2O_3, a certain amount of Y ions substitute Zr ions leaving behind some oxygen vacancies (by removing O ions) to keep the electrical neutrality of the system. The correct placement of ions at the GB region is crucial to ensure that the GB structure is stable. We used the protocol described in Ref. [47] to create the initial configuration of the ZrO_2 bi-crystal model, as shown in Fig. 1(a). It consists of two single crystals of cubic ZrO_2 with a tilt angle of 36.9°. The introduction of periodic structure of the bi-crystal model in the *x* direction results in two $\sum 5(310)/[001]$ grain boundaries between the two single crystals. The dimension of the bi-crystal is 11.5nm, 5.8nm, 5.4nm along *x, y* and *z* axis, respectively. Note that the dimension of the bi-crystal model expands slightly with the increase of temperature. The *x* axis is perpendicular to the GB planes. The two GBs are separated by a distance of 5.2nm, which is sufficiently large to avoid any non-physical interactions between the GBs [48].

Based on the initial configuration in Fig. 1(a), we substitute 16% of Zr ions by Y ions to create the 8mol% Y_2O_3 stabilized ZrO_2, i.e., the 8YSZ bi-crystal model, following the Eq. (1) for achieving charge neutrality in the system [38,45,46,49,50].

$$Y_2O_3 + ZrO_2 \rightarrow 2Y'_{Zr} + V_O^{\cdot\cdot} \quad (1)$$

Note that, in order to achieve sufficient statistical randomness of the Y ions, we created a large size of model consisting of ~30,000 ions, in contrast to published models with typically less than ~3,000 ions. This is also to avoid the necessity of averaging multiple models for sufficient statistics. Then, MD modeling of energy minimization for the 8YSZ system is carried out, as the resultant atomic structure is shown in Fig. 1(b) where the Y ions are randomly distributed across the model. Note that, as a result of charge balancing via Eq. (1), the initial configuration of the 8YSZ bi-crystal system contains about 2.7at % oxygen vacancies. The nominal compositions of each type of ions in the bi-crystal model are listed in Table 1 (see Section 3.1). In addition, experimental observations have indicated that the segregation of ions mostly concentrated nearby the GB plane spanning half-width of 0.6nm on both sides [50], as the GB regions indicated in Fig. 1(b). The rest of the bi-crystal model is considered as grain interiors or bulk regions.

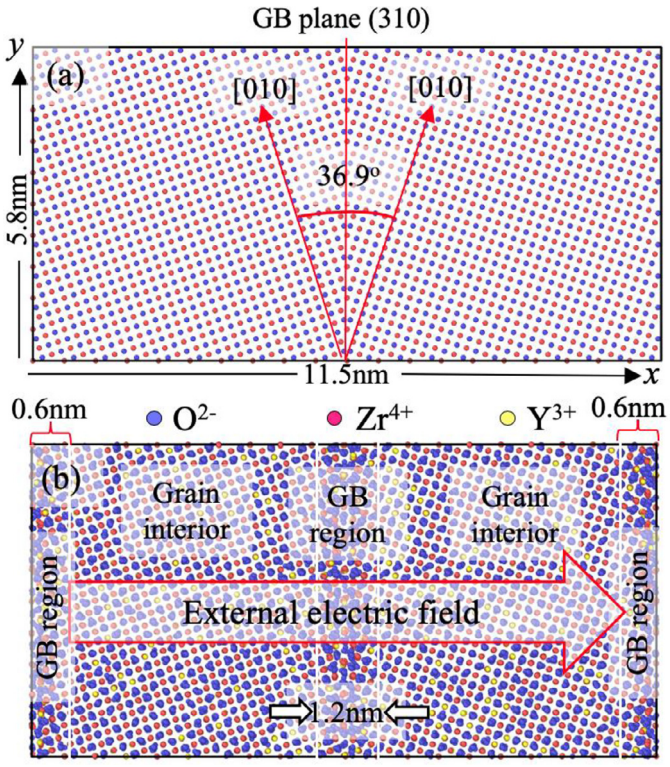

Fig. 1. Bi-crystal model for the $\Sigma 5(310)/[001]$ grain boundary: (a) ZrO_2 initial configuration; (b) 8YSZ structure after MD energy minimization. The direction of the external electric field is perpendicular to the GB plane.

Table 1
Concentrations of different ions in the 8YSZ bi-crystal model after MD equilibration.

Types of ions	Nominal concentration (at%)	GB region concentration (at%)	Grain interior concentration (at%)
Y	5.6	6.1 ± 0.1	5.3 ± 0.1
Zr	28.7	28.6 ± 0.1	28.7 ± 0.1
O	65.7	65.3 ± 0.1	66.2 ± 0.1

2.2. Computational details

2.2.1. Interatomic potential and the coupling of E-field

We use MD simulations to compute the ionic diffusivity as a function of temperature (T) and E-field (E). At a given temperature, incorporating E-field into MD simulations for an ionic system can be achieved by adding a force F=qE to each ion with a charge of q [51]. The interaction potential $V(r_{ij})$ between ions *i* and *j* can be well modeled by a Buckingham type function (1st and 2nd terms on the right) coupled with a long-range Coulombic term (3rd term on the right):

$$V(r_{ij}) = A_{ij} exp\left(-\frac{r_{ij}}{\rho_{ij}}\right) - \frac{C_{ij}}{r_{ij}^6} + \frac{1}{4\pi\varepsilon_0}\frac{q_i q_j}{r_{ij}} \quad (2)$$

where r_{ij} is the interionic distance between ions *i* and *j* with the respective charge of q_i and q_j. ε_0 is the dielectric constant of vacuum. The parameters A_{ij}, ρ_{ij} and C_{ij} for the 8YSZ crystal are taken from the literature [35,36]. This set of parameters with integer charges for the ionic species predicts the static and dynamic behavior of YSZ crystals consistent with experiments [37,38]. Our MD simulations were carried out using the LAMMPS code – one of the most widely used molecular dynamics software [34].

2.2.2. Diffusion coefficient and activation energy of diffusivity

Based on the MD trajectories, the diffusivity (D) of ions can be obtained from the mean square displacement (MSD) calculations according to the Einstein relation [52,53],

$$D = \frac{1}{6N_m t}\lim_{t\to\infty}\left\{\sum_{j=1}^{N_m}\left[r_j(t) - r_j(0)\right]^2\right\} \text{at constant T \& E} \quad (3)$$

Eq. (3) represents an ensemble average over time t of all ions from j=1 to N_m. The initial $r_j(0)$ and dynamic $r_j(t)$ positions are given by the MD trajectories. Since one already observes that the calculated MSD is proportional to t at relatively short simulation times (<a few tens of nanoseconds) [52,53], this makes MD a very cost-effective computational technique to obtain diffusion coefficients. Note that the bi-crystal model is divided into GB and grain interior regions (see Fig 1b). We have calculated the MSDs for ions within each region, which yielded the corresponding diffusion coefficients via Eq. (3). Also, in our simulation, 5-10ns simulation time in the MD runs was used to generate MD trajectories at different temperatures. The last 3-5ns of the MD trajectories were used for the ensemble averages of MSDs to compute the diffusion coefficients, ensuring sufficient accuracy in the statistical analysis.

Furthermore, based on the above diffusivity results, we can obtain the activation energy (Q) for the atomistic mass transport or diffusion, in the same manner as is done in experiments using Eq. (4) [54,55]

$$D = D_0\exp\left(\frac{-Q}{RT}\right) \quad (4)$$

D_0 is the pre-exponential factor and R is the gas constant. The common practice of using Eq. (4) is to plot the Arrhenius plots of diffusivity against inverse T, from which the Q can be easily determined as the plot's slope. After running a series of MD simulations at varied applied electric field E for different temperatures, the diffusion coefficient and its corresponding activation energy as a function of T and E can be obtained with the coupling of Eq. (3) and Eq. (4).

2.2.3. Point defect quantification

We use the Wigner-Seitz (WS) cell method to identify the vacancy and interstitial point defects in the 8YSZ bi-crystal model. In particular, we focus on the quantification analysis of vacancies of cations and anions as well as the cation vacancy-interstitial pair Frenkel defects, since they are reported to be the main factors determining the flash sintering rate of YSZ systems [1,19,28]. The WS cell method has been implemented in one of the most widely used scientific visualization and analysis software for atomistic and particle simulation data – Open Visualization Tool (OVITO) [56]. In general, the WS cell method requires two configurations of the atomistic system as inputs: the reference configuration (initial structure) and the displaced configuration (MD trajectories). The reference configuration defines where ions would be located in a defect-free state of the crystal. Thus, typically this is a perfect crystal lattice (e.g., Fig. 1a) where every site is occupied by exactly one ion. The displaced configuration (e.g., equilibrated structures) is the one to be analyzed, which typically contains some point defects. The WS cell method determines which ions occupy what sites. Some sites may be occupied by no ions at all – the vacancy point defects. Moreover, WS cell method can identify whether a vacancy is cationic or anionic in the system, which is especially convenient for this work because different types of vacancies contribute to ionic diffusivity in the YSZ via different ways. Note that we average the counting of vacancies over the last 3-5ns MD trajectories out of the 5-10ns MD runs for sufficient statistics.

2.2.4. Charge density and electrostatic potential

The spatial distribution of the charge density (ρ) in the bi-crystal model can be directly obtained from the summation of positive and negative charges per unit volume. Then, by integrating twice the charge density profile according to Poisson's equation of Electrostatics (Eq. (5)), which relates the electrostatic potential to charge density [57], we can readily compute the corresponding electrostatic potential (φ). In this work, we compute the one-dimensional (1D) profiles of the charge density and potential across the x direction (perpendicular to the GB plane) of the bi-crystal model, which provides sufficient insight to the GB space charge of the YSZ system.

$$\nabla^2\varphi = -\frac{\rho}{\varepsilon_0} \quad (5)$$

where ε_0 is the permittivity of free space (vacuum).

2.2.5. MD simulations

Prior to the introduction of E-field, the model needs to be sufficiently equilibrated at specific temperature and pressure, during which GB segregation and new formation of various types of point defects, including vacancies and interstitials, are expected to occur. For example, an equilibrized 8YSZ bi-crystal model can be achieved under NVE conditions at 10K and 1atm for 1ns followed by NPT conditions at 1500K and 1atm for 5ns. Note that the MD simulation step is set to be 1fs throughout the MD modeling in this work. Based on the equilibrated structure at 1500K and 1atm, other equilibrated models at higher temperatures (and 1atm) can be readily obtained using NPT modeling for 3-5ns. Periodic structures at the boundaries of the bi-crystal models are introduced at all the three x, y, and z directions. These equilibration modelings lead to changes in the ionic positions and certain levels of ionic segregations in the vicinity of grain boundary planes (details refer to Table 1 in Section 3.1).

Starting from the pre-equilibrated 8YSZ bi-crystal models at different temperatures of 1500K, 2000K, 2500K, and 3000K, we performed 5ns MD runs with NPT conditions at 1atm corresponding to different temperatures. Furthermore, for each temperature, the bi-crystal model was subjected to different electric field strengths of 50V/cm, 100V/cm, 500V/cm, and 1000V/cm with the E-field perpendicular to the GB plane (see Fig. 1b). A total number of 20 different MD NPT simulations were carried out. The 5ns simulation time for each case ensures sufficient dynamics and diffusion of ions for the accurate computation of diffusion coefficients. Subsequently, using Eq. (3), the temperature and E-field dependences of diffusivity of ions in 8YSZ were obtained from the MD trajectories.

3. Results

3.1. GB segregation and space charge in the absence of E-field

The realistic model representation of experimentally observed bi-crystal GB structure is vital to compute the GB diffusion coefficients accurately. In the case of YSZ GB, it is well known that Y ions segregate within a layer of a couple of nanometers thick surrounding the GB planes, accompanied by significant oxygen deficiency nearby the GB plane [50]. As a consequence, a positive electrostatic potential across the YSZ GB is formed. It is called the double layer or GB space charge of segregation [58]. The value of this potential is reported to be largely scattered across the range of ~0.1-1.2V [50,58,59].

Fig. 2 presents the one-dimensional (1D) concentration profiles of Y, Zr, and O ions along the x direction (normal to the GB plane) of the 8YSZ GB model after the MD equilibrium modeling. Note that the reduced distance denoting the ratio between the x position and the length of the simulation box at x direction is used to

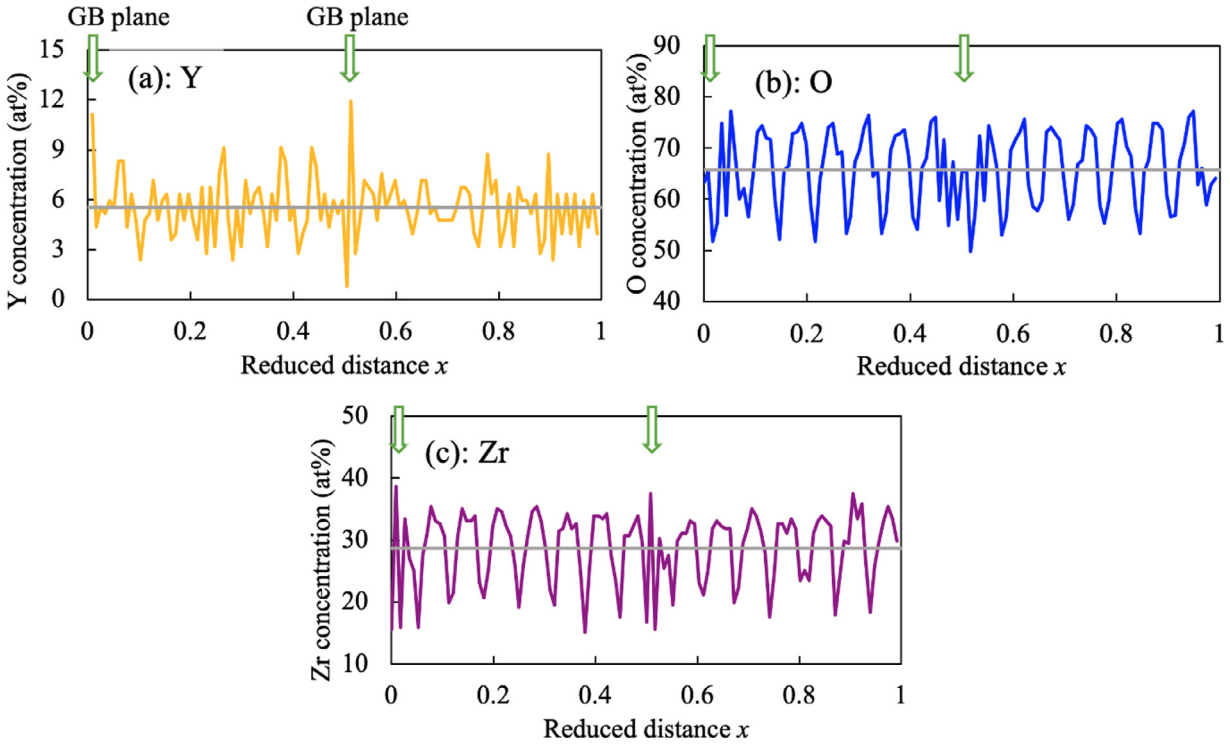

Fig. 2. Concentration profiles along the *x* direction (normal to GB planes) as a function of reduced distance for various ions: (a) Y, (b) O, and (c) Zr.

plot the concentration profiles. The nominal concentrations of each type of ion are indicated by the horizontal lines in Fig. 2 and listed in Table 1.

Apparent segregation of Y ions (Fig. 2a) and deficiency of O ions (Fig. 2c) near the GB planes are observed in the 8YSZ bi-crystal model. No significant depletion of Zr ions is observed. Note that the fluctuation observed in the concentration profiles is due to the local environmental change in the atomistic chemistry of the periodic lattice of the crystal. Moreover, Table 1 lists the statistical concentrations of different ions at the GB regions and grain interiors in the model, comparing to their nominal concentrations. The Y ion concentration at the GB regions is ~0.8at% (=6.1at%-5.3at%) greater than that in grain interiors. This is somewhat lower than the experimental measurements, which suggested a ~1-2at% higher Y ion concentration at the GB region as compared to grain interior in the 8YSZ Σ5(310)/[001] bi-crystal [60].

There are two mechanisms driving the ionic segregation when two YSZ single crystals meet to form a GB. These are the significant elastic mismatch, which provides a large driving force for immediate Y ion segregation nearby the GB plane due to the dissimilarity between the ionic radii of the Zr ion (0.84Å) and Y ion (1.02Å) [45]; and the Coulombic interactions between the various chemical species, which depends on the arrangement of the charges nearby the GB plane. We believe the GB segregation observed in our MD modeling is mostly due to the GB misfit elastic energy, with Coulombic interactions playing a secondary role; this situation, which has been modeled theoretically elsewhere [58], has been previously reported for this system [45]. A significantly longer simulation time (>>ns) is needed to achieve the experimental level of GB segregations, which is not practical using MD simulations. This is probably why our MD modeled Y ion segregation is lower than experimental measurements. Interestingly, Meléndez et al. [37,45] developed a strategy to artificially impose a driving force specifically onto the Y ions within a chosen GB region to facilitate the GB ionic segregations. However, one critical requirement of this approach is the pre-knowledge of the accurate

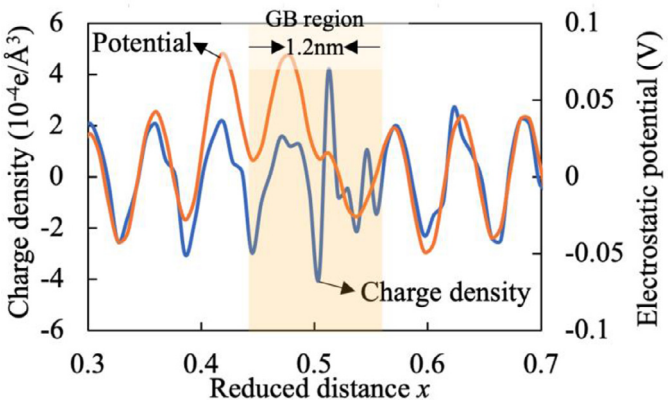

Fig. 3. Charge density distribution and electrostatic potential profile at zero E-field vs. the reduced distance in the *x* direction (T=3000K).

determination of GB segregation energy or driving force as a function of temperature, which is usually not readily available from experiments. Furthermore, to the best of our knowledge, there is no GB segregation energy under the presence of an external electric field reported in the literature for the YSZ system.

Fig. 3 displays the 1D distribution of charge density and electrostatic potential as a function of reduced distance at the *x* direction across the bi-crystal model. A clear localization of charge density is observed at GB regions. By integrating twice based on the charge density profile using Eq. (5), we obtained a positive electrostatic potential of about 0.08V in the vicinity of the GB plane, which is reasonable as compared to the reported experimental measurements [50] and theoretical calculations [58].

3.2. Effect of E-field on diffusion coefficients of ions

To further verify the reliability of our modeling, we compare our MD computed diffusivities of the three types of ions in the sys-

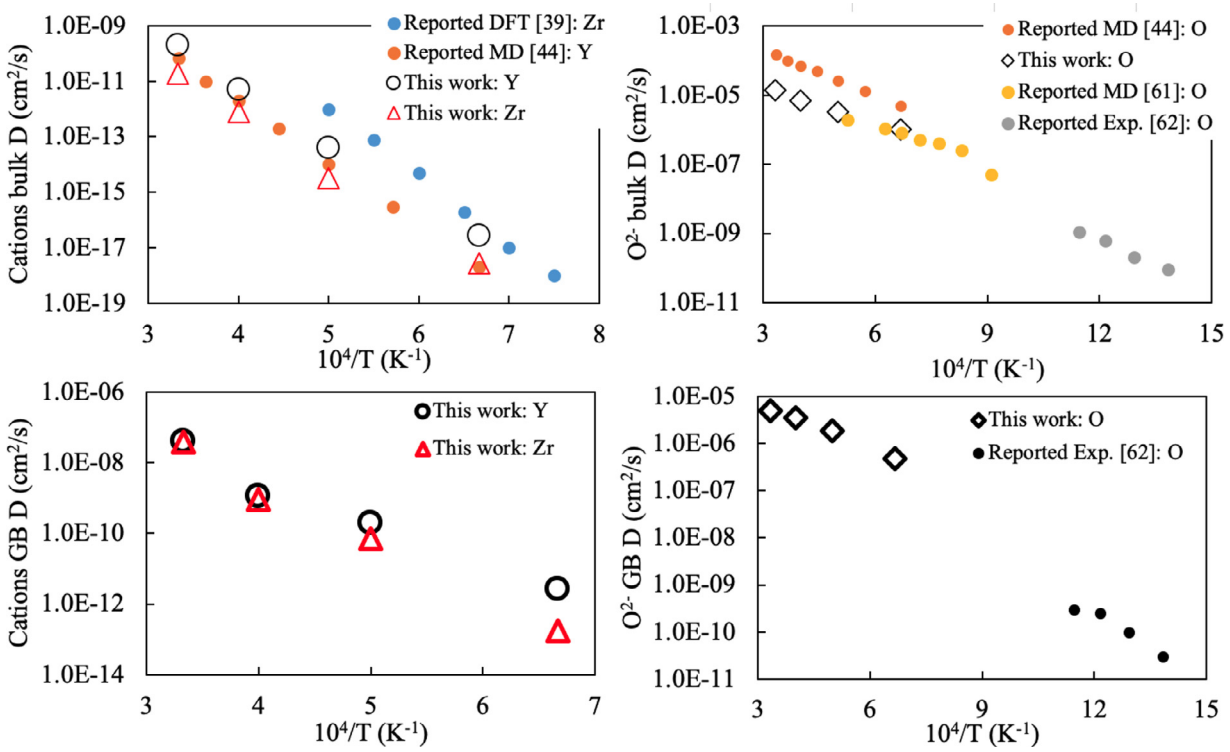

Fig. 4. Arrhenius plots for bulk and GB diffusion of cations and anions in the 8YSZ system in the absence of E-field: comparisons between MD results from this work (open shapes) and the reported experimental and simulation data (closed circles).

Table 2
Comparison between present MD calculated activation energies (at zero E-field) for bulk and GB diffusion of various ions in the 8YSZ system and data taken from the literature.

	ions	E_A (eV): this work	E_A (eV): reported
bulk	O	0.62 ± 0.10	0.87 [44]; 0.77 [61]; 0.93 [62]
diffusion	Zr	4.09 ± 0.20	4.89 [39]
coefficients	Y	4.05 ± 0.20	4.44 [44]
GB	O	0.66 ± 0.10	0.86 [62]
diffusion	Zr	3.04 ± 0.20	/
coefficients	Y	2.34 ± 0.20	/

tem with experimental and simulation data published elsewhere. Fig. 4 shows the Arrhenius plots of the bulk and GB diffusion coefficients of O, Zr, and Y ions with the absence of E-field, i.e., E=0V/cm. The agreement between our MD results and the reported evidence is satisfactory. As listed in Table 2, we also compare the obtained activation energies of diffusivity with existing data, and our results lie within the range of published values.

Fig. 5, Fig. 6 and Fig. 7 present the bulk and GB diffusivities as a function of temperature (1500K-3000K) and E-field (up to 1000V/cm). First of all, the temperature dependence of diffusion coefficients varies over a much broader range of values than the E-field dependence. Take the Y GB diffusivity as an example (see Fig. 5b), at any constant E-field, the diffusivity increases by 4-5 orders of magnitude as the temperature changes from 1500K to 3000K. Whereas, at any constant temperature, the diffusivity increases only by about one order of magnitude at E-field is increased up to 1000V/cm. This suggests that, within the parameter ranges under consideration, the thermal energy is a more dominant factor of ionic diffusivities in YSZ as compared to E-field. Also, as shown in Figs. 5 and 6, in the case of cations, GB diffusivity is ~2-5 orders of magnitude higher than the bulk diffusivities at a constant temperature and E-field, which is expected as the GB defect is known to be a fast diffusion path. Moreover, the apparent effect of E-field on both the bulk and GB diffusivities is observed for the two cations. As the E-field increases from 0V/cm to 1000V/cm, both the bulk and GB diffusion coefficients are increased by about one order of magnitude at any given temperature.

In the case of anions, shown in Fig. 7, there is no obvious difference between bulk and GB diffusivities. This is probably due to the presence of a space charge layer surrounding the GB plane, hindering the O ion diffusion along the GB plane. Also, no considerable effect of E-field on the bulk O ion diffusion is observed (see Fig. 7a). However, a more significant effect of E-field on the GB O ion diffusivity is detected, as shown in Fig. 7b. The O ion GB diffusion coefficient is increased by 2-3 times when the E-field is increased to above 500V/cm.

As described above, even though the influence of E-field (<1000V/cm) on the diffusion coefficient is less effective as compared with thermal energy, it does contribute to the enhancement of ionic diffusivity for all the cations and anions. This enhancement may be attributed to two factors: the E-field induced formation of new vacancies, and the reduction of the electrostatic potential or space charge at the GB region disrupted by the E-field. These effects will be discussed in the following Sections.

3.3. Effect of E-field on vacancies

The nominal total concentrations of vacancies (C_{Vac}) and interstitials (C_{Int}) throughout the bi-crystal model were computed for each given E-field at different temperatures. All of the 20 MD modeling results are shown in Fig. S1 in the Supplemental Material. In each case, the subtraction of vacancies from interstitials resulted in exactly the same value as the concentration of pre-existing O vacancies, i.e., C_{Vac}-C_{Int}=2.7%. This indicates that the total number of newly formed vacancies (of Y, Zr, and O ions) and interstitial (of Y, Zr, and O ions) point defects maintain the same throughout the

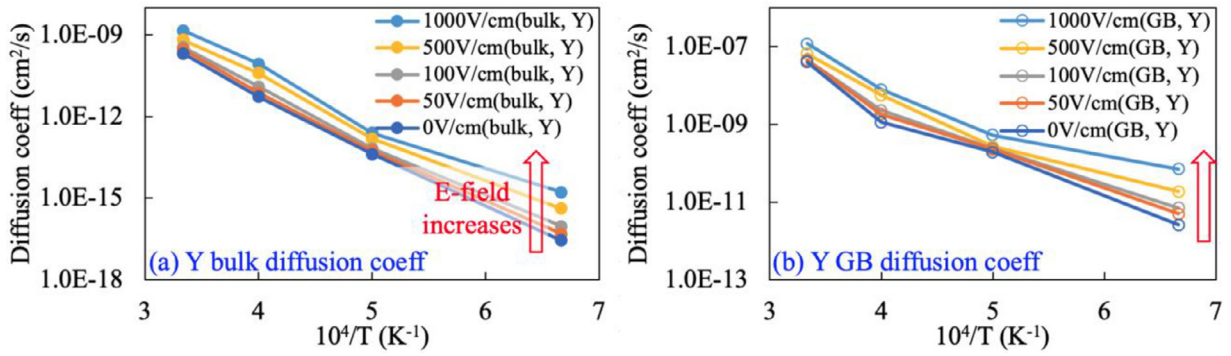

Fig. 5. Arrhenius plots of (a) bulk and (b) GB diffusivity of Y ions for E-field up to 1000V/cm.

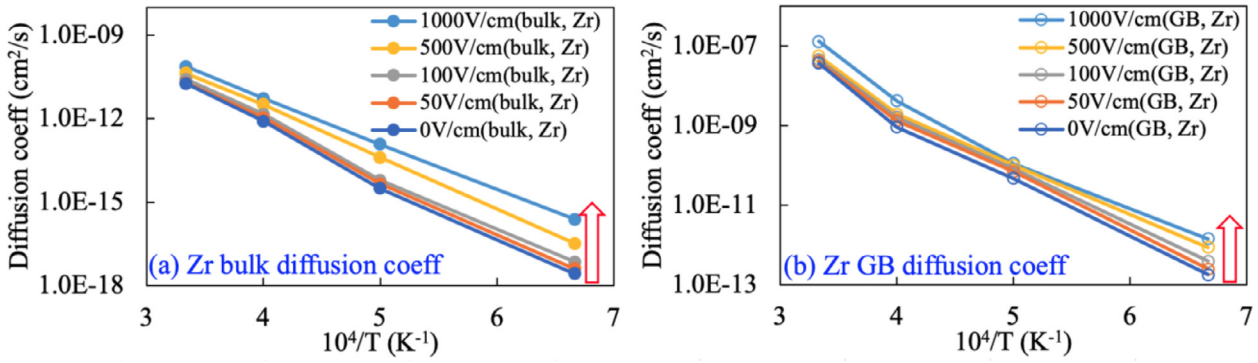

Fig. 6. Arrhenius plots of (a) bulk and (b) GB diffusivity of Zr ions for E-field up to 1000V/cm.

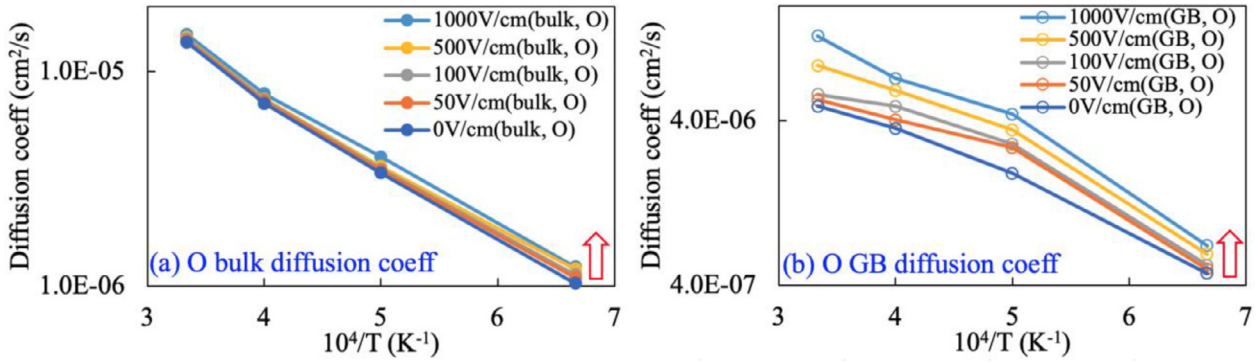

Fig. 7. Arrhenius plots of (a) bulk and (b) GB diffusivity of O ions for E-field up to 1000V/cm.

MD modeling at a given temperature and E-field. This reveals an important observation that the E-field induces the new formation of Frenkel pair defects in the 8YSZ system.

Fig. 8(a,b) and (c,d) show the respective concentration (at%) at GB and grain interior for vacancies of cations and anions as a function of E-field at different temperatures. Note that the cation vacancy V_{Zr} in YSZ can be used for the diffusion of both Zr and Y ions [63]. First of all, at a given E-field, vacancy concentration increases with the increase of temperature. Secondly, in both cases of cation and anion, the vacancy concentration at GB is a few times higher as compared to the grain interior (bulk) counterpart. This is due to the semi-ordered or disordered GB structures favoring the formation of vacancies under thermal and/or E-field activations. It is also in good agreement with the Y ion segregation to the GB, which is expected to rearrange the chemical species to minimize the elastic misfit effect and screen the additional charges. Thirdly, at a given E-field, in the grain interior region, the cation and anion vacancy concentrations do not change considerably when the temperature is increased to 2000K, then increase drastically with the further increase of the temperature. Interestingly, our observation that the E-field does not induce an appreciable amount of formation of cation Frenkel pairs in the grain interior or bulk region at a relatively low temperatures, is in line with the results reported by Schie et al. [64]. In contrast, the cation and anion vacancy concentrations at the GB region increase significantly with the increase of temperature starting from 1500K. Apparently, the formation energy for vacancies at the GB region is lower than that in the bulk region in the 8YSZ bi-crystal system.

The most striking observation in Fig. 8 is that cation vacancy concentration is more sensitive to the E-field as compared with that for anion vacancies, especially at GB region and/or at higher temperatures (>2000K). It should be noted that the formation of cation vacancies is accompanied by that of an equal amount of cation interstitial defects at any E-field and temperature, i.e., the cation Frenkel pair defects form at all external conditions (also see Supplemental Material). On the contrary, anion vacancy concentration does not vary obviously with the change of E-field at a given temperature. This may be partially due to the larger elec-

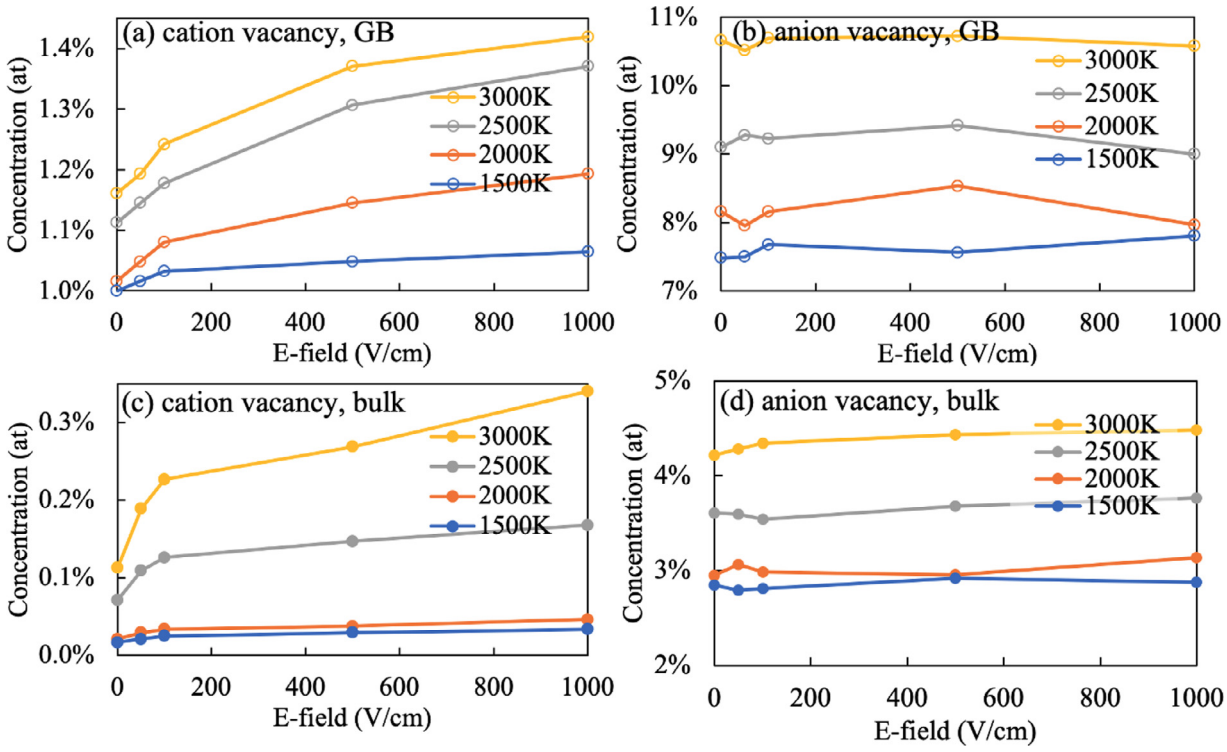

Fig. 8. Concentrations (at%) of cation and anion vacancy point defects as a function of E-field at different temperatures at GB (a, b) and in grain interior or bulk region (c, d).

trostatic forces (F=qE) exerted onto cations (q^{Zr}=4+, q^{Y}=3+) that have higher charges than that of the anions (q^{O}=2-). We think that the mechanisms for GB diffusion are different for anions and cations, which causes the enhancement of their diffusion coefficients. For cations, diffusion is dominantly assisted through the formation of new vacancies. In contrast, the increased diffusivity of anions is probably achieved due to variation in the GB space charge, which will be further elucidated in Section 3.4.

The sintering rate of 8YSZ is largely determined by the diffusion of cations, i.e., Zr and Y ions, because of their slower diffusion rates than that of anions. We thus performed further analysis to quantify the influence of E-field on the formation of new Zr and Y vacancies. We have quantified the formation of new vacancies by defining a temperature-dependent enrichment factor f_T, defined as:

$$f_T = \frac{C_{vac}^{E}}{C_{vac}^{E=0}} \tag{6}$$

where C_{vac}^{E} is the vacancy concentration at a given E-field and $C_{vac}^{E=0}$ is the initial vacancy concentration, calculated at E=0V/cm.

Fig. 9 shows the f_T for Y and Zr ions as a function of E-field at different temperatures. As shown in Fig. 9(a), f_T reaches ~1.45 at E-field=1000V/cm and T=3000K, indicating the cation vacancy concentration of Y ions at GB is increased by up to ~45% (with a standard error of ±10%). Note that the vacancy concentration for each case was averaged over the last 3-5ns MD trajectories out of the 5-10ns MD runs. In contrast, as shown in Fig. 9(b), a relatively less significant influence of E-field on the Zr ion vacancy concentration at GB is observed, especially at lower temperatures.

We also computed the f_T of Y and Zr vacancy concentrations at different temperatures in the grain interior (see Fig. 9c and d). There is up to ~300-400% (with a standard error of ±100-200%) increase in the Y and Zr vacancy concentrations in grain interior when the E-field is ≳500-1000V/cm. Note that the very high standard error is because that only a small number of cation vacancies are formed in the bulk regions (1-3 orders of magnitude less than that formed at GB regions). Consequently, any small variation in the counting of cation bulk vacancies during MD runs would cause a relatively large variation in the vacancy concentration, which gave a large standard error. A much larger configuration with the number of ions >>30,000 is needed, which is not cost-effective for MD modeling of YSZ systems.

3.4. Effect of E-field on GB space charge

Fig. 10 shows the charge density and electrostatic potential at different levels of E-field at the GB region, calculated at T=3000K. As seen in Fig. 10(a), the charge density at the GB region is reduced with the increase of E-field. This suggests that the space charge at GB should also decrease in the 8YSZ system [65]. Furthermore, the electrostatic potential at the GB region is also clearly affected by the E-field. For example, as the E-field is increased to 1000V/cm, the difference of electrostatic potential at GB region (between 0.48 and 0.54 of the reduced distance *x*, see Fig. 10b) decreases from ~0.1V=0.08V−(−0.02V) to ~0.07V=0.03V−(−0.04V), as indicated by the lengths of the vertical solid lines in Fig. 10b.

We speculate that the reduction in GB space charge contributes to enhancing the O ion diffusivity at the GB region through local structural modification at the atomistic level. In the YSZ system, it is common that Y ions are associated with O vacancies through an association interaction; such an interaction can be significant when the concentration of Y ions is high [66]. At E-field=0, the Y ions segregation at the GB region results in a high probability of the formation of $Y'_{Zr}V_{\ddot{O}}$ defect pair. At E-field>~500-1000V/cm, the significantly increased cation vacancy and diffusivity at GB regions may increase the disordering of GB atomic structure and weaken the interaction of $Y'_{Zr}V_{\ddot{O}}$ defect pair, thus, accelerating the dynamics and diffusivity of O ions at the GB region (see Fig. 7b). This also explains that little increase in the diffusivity of O ions in the grain interior region (see Fig. 7a) due to the lack of new forma-

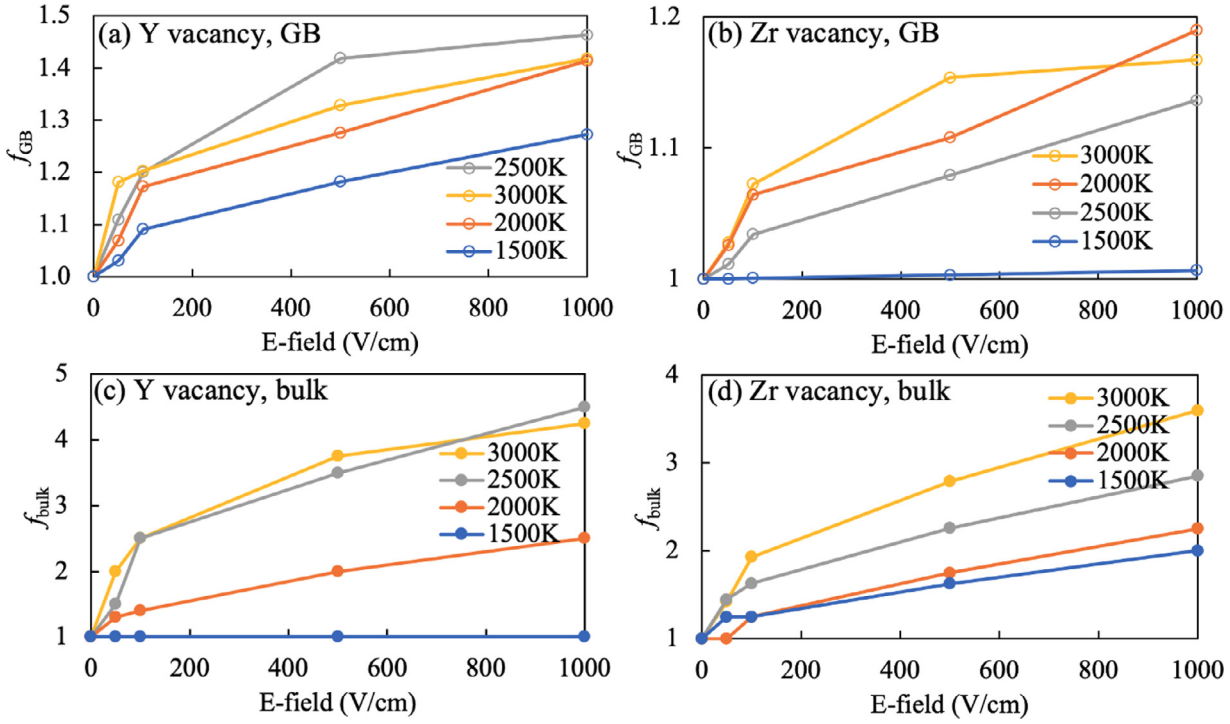

Fig. 9. The enrichment factor f_T of Y and Zr vacancy concentrations at GB (a, b) and in grain interior or bulk region (c, d).

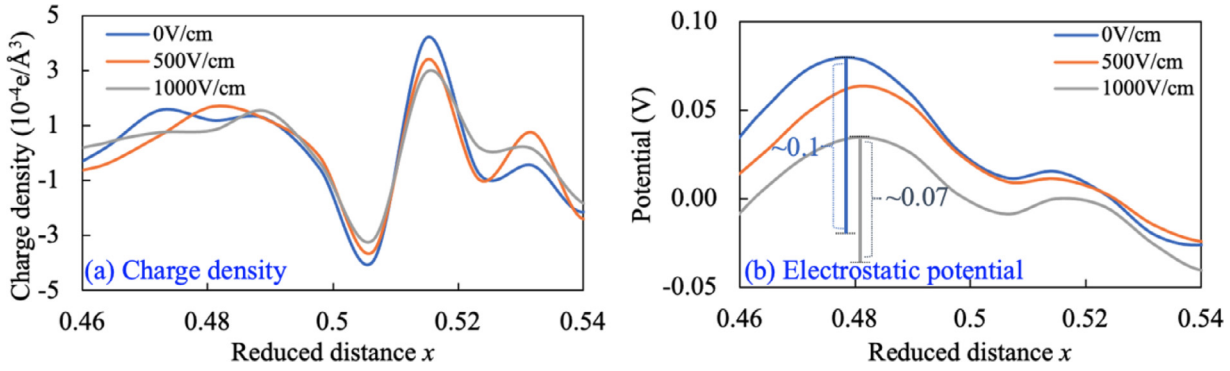

Fig. 10. E-field dependent GB charge density and electrostatic potential profiles at T=3000K.

tion of substantial amount of cation vacancies at grain interior region. Further studies and experimental (e.g., high-resolution transmission electron microscopy – HRTEM) evidence on the correlation between the increased GB disordering and O ion diffusivity are needed to understand better the GB space charge and its influence on the O ion diffusion, which will be the authors' future work.

4. Discussions on the contribution of non-thermal (E-field) mechanism of flash sintering

As indicated by the results presented in Sections 3.3 and 3.4, there is a significant increase in the number of new vacancies of cations and a reduction of the electrostatic potential of GB space charge in the 8YSZ system when an intense external E-field (≳500-1000V/cm) is applied. As a result, the diffusions of cations are largely boosted (see Section 3.2), which is expected to greatly enhance the rate of mass transport during the flash sintering process. The enhanced diffusivity of ions in 8YSZ due to the E-field verifies previous assumptions on the flash sintering mechanism in the literature. For example, R. Raj et al. proposed that the sufficiently high E-field and temperature in ceramic samples during flash sintering may act synergistically to produce the formation of an avalanche of new defects [67]. Our preliminary quantifications of such defect avalanche in the 8YSZ system are displayed in Fig. 9. Also, J. Narayan et al. reported that the interaction between cation and anion vacancies with the elastic and electronic fields increases the diffusion rates along dislocations and grain boundaries during the oxides flash sintering [30].

Interestingly, H. Majidi and K. van Benthem [26] reported in their in-situ scanning transmission electron microscopic (STEM) experiment that sudden shrinkage and sintering of 3YSZ powder agglomerates happened when an E-field of 500V/cm is applied (at a threshold temperature of 900°C). It should be noted that the E-field in their experiments is introduced without allowing the touching of electrodes and the sample, i.e., any electric current is absent during the sintering process. This is in contrast to typical flash sintering where the electrodes are in direction/physical contacting with the samper powders (compacts) [19]. They further assumed that the applied E-field lowers the activation energy for point defect formation within the space charge zone and hence, promotes neck formation and consolidation. Based on the diffusiv-

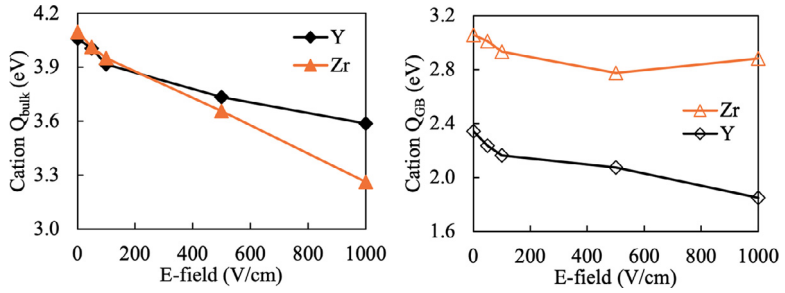

Fig. 11. Activation energy of diffusion (Q) for cations (Y, Zr) as a function of E-field at grain interior or bulk (a) and GB (b) in the 8YSZ system.

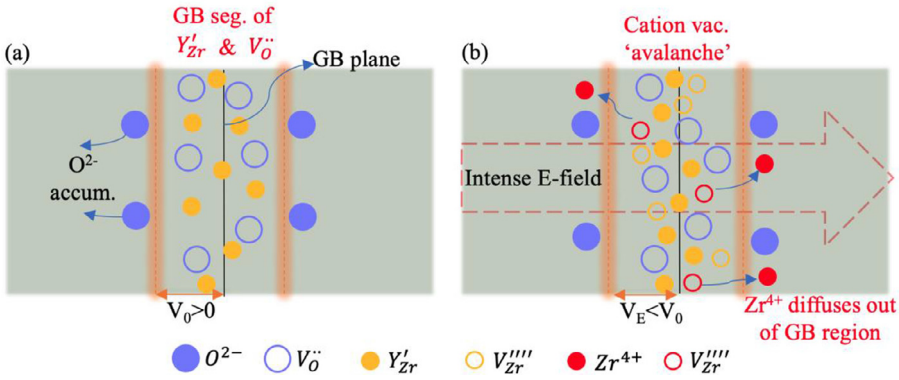

Fig. 12. Schematic diagram of GB structure and space charge: (a) E-field=0V/cm, (b) E-field ≳500-1000V/cm. Note that only ions/vacancies contribute to the GB space charge are emphasized. The relative number of ions/vacancies is not proportional to the realistic bi-crystal system.

ity results in Figs. 5 and 6 in this work, by using Eq. (4), we also computed the activation energy (Q) of diffusion for cations as a function of E-field at GB and grain interior, as the results shown in Fig. 11. In general, activation energy decreases by ~5-20% when the E-field reaches 1000V/cm. Thus, our MD modeling predictions on the diffusivity and activation energy agree with the in-situ STEM observations.

Based on results in Section 3 and the above discussions, we propose the following atomistic explanation of enhanced GB diffusivity of ions under the intense E-field, as a possible contribution of non-thermal (E-field) mechanism of flash sintering for YSZ systems. As shown in the schematic diagram in Fig. 12(a), in the absence of E-field, there exists co-segregation of O vacancies ($V_O^{\cdot\cdot}$, light blue open-circles) and Y ions (Y'_{Zr}, orange closed-circles) in the vicinity of the GB plane. The accumulation of O ions outside of the GB region results in the formation of GB space charge layer, which has a positive potential, e.g., E_0=0.08V for the 8YSZ $\sum 5(310)/[001]$ GB at 3000K.

However, as depicted in the schematic diagram in Fig. 12(b), the applied intense E-field (≳500-1000V/cm) creates a number of new cation vacancies (V''''_{Zr}), mainly at the GB region, which appears as Zr ions diffusing outside the GB region. This was previously called defect 'avalanche' in the literature [67] and confirmed by our MD modeling (see Fig. 9). The effectively negative charges of cation vacancies present at the GB region reduce the local electrostatic potential or the GB space charge, i.e., V_E<V_0 at an intense E-field. The increase in the concentration of cation vacancies causes boost diffusivity of cations, thus facilitating the flash sintering process. In contrast, anion vacancy concentration at GB is nearly independent of the E-field. One of the reasons why the effect of E-field is more significant on cations than on anions is possibly due to the larger electrostatic forces (F=qE, q is the charge) acted on cations due to their higher charges. However, the exact reasons need to be further investigated, which is our next-step research focus. Additionally, the substaintial enhancement of diffusivity by an intense E-field (>~500-1000V/cm) during flash sintering is expected to boost the grain growth kinetics. For example, a recent work by Ren et al., detected faster grain growth for higher E-field during flash sintering of 3YSZ [68]. Thus, the main factor that allows fabrication of fine-grained materials by flash sintering is the short processing time.

As discussed in Section 3.3, at a given temperature, when the E-field≳500-1000V/cm is introduced in the model, we only observed the significant formation of cation Frankel pairs at GB regions. No appreciable amount of new anion vacancies is formed due to the E-field at any temperature. Furthermore, the GB space charge decreases with the E-field, suggesting the existence of additional negative charges diffused into the GB regions, e.g., V''''_{Zr}. We thus conclude that the E-field-induced point defects mainly exist in the form of cation (zirconium) Frenkel defects in the YSZ system. Thus, our results are in line with the previous assumption that Frenkel pair defects may form in the YSZ material system during the FS process [24]. It was further suggested in the literature that vacancies are preferentially driven into the grain boundaries and the interstitial ions into the pores, facilitating densification by flash sintering process [69,70].

It should be noted that no significant preferential ionic movements along the direction of E-field are observed within the simulation time (<5-10ns) of MD runs, even in the case where E-field=1000V/cm and T is just below T_m≈3079K ([71]). This agrees with Raj's observation that electrodes (e.g., platinum [19]) are, in fact, transporting electrons, not oxygen ions, during the flash sintering process. In particular, at 1000V/cm and 3075K, the MSDs of O ions at grain interior (bulk) and GB regions as a function of simulation time are shown in Fig. 13. Note that the last 4ns MSDs from a 5ns MD run are presented, where the slopes of the MSDs are clearly linear. In both cases, ionic displacements are observed in all three directions of *x, y, z* axis, as indicated by the blue, orange and grey curve, respectively. Note that O ions diffuse at approximately the same rates in both grain interior and GB regions, as indicated by the similar levels of MSD values at GB region and in grain interior.

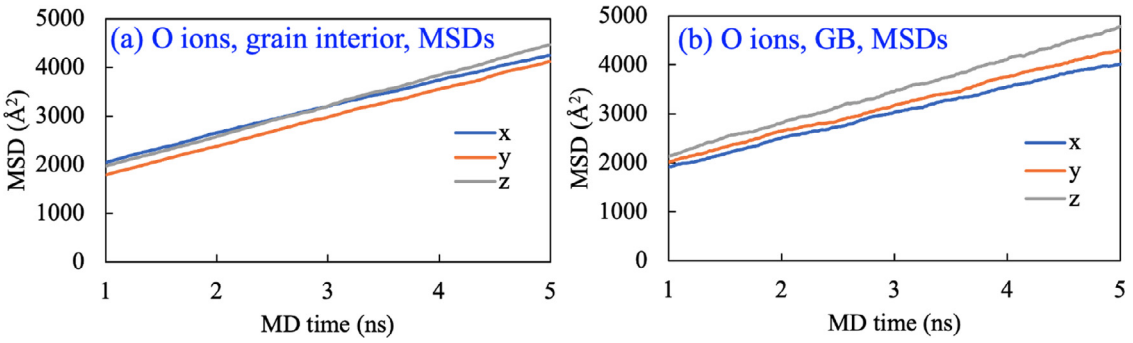

Fig. 13. MSDs of O ions at grain interior (a) and GB regions (b) in the 8YSZ system at 1000V/cm and 3075K.

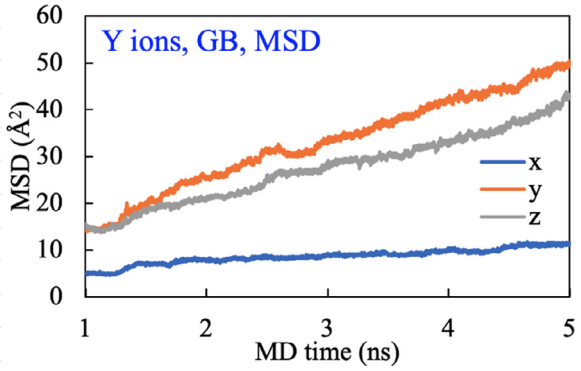

Fig. 14. MSDs of Y ions at the GB regions in the 8YSZ system as a function of simulation time (for 5ns) at *x*, *y*, *z* directions at 1000V/cm and 3075K.

A slightly different diffusion phenomenon was observed for cations. Taking the GB diffusion of Y ions as an example, no significant displacement along *x* axis (E-field direction, see Fig. 1) is observed within 5ns simulation time, as indicated by the MSDs shown in Fig. 14. This result is also in line with the theory of ionic conduction in ceramics, which suggests that an E-field of <1000V/cm does not provide substantial driving force to induce significant preferential migration of ions along the field direction. Instead, it provides a small perturbation to the ionic dynamics. For instance, the E-field-induced energy change for ionic diffusion ($\frac{1}{2}zeEd$, where z is the charge of the ion, e is the unit charge, and d is the lattice parameter) [72] is estimated to be about four orders of magnitude smaller than that of the thermal energy (kT, where k is the Boltzmann's constant) for 8YSZ under 1000V/cm at elevated temperatures. Furthermore, Y ions diffuse mostly along the GB plane, i.e., along the *y*-*z* plane perpendicular to the E-field direction, which makes sense because GBs are known to be fast channels for atoms to diffuse [54]. Interestingly, J. Luo [8] and I.-W. Chen [39,73] reported significant ionic migration during the flash sintering process. Our MD findings and the critical results reported by Luo and Chen suggest that, in fact, the electrical current during the flash sintering process of the YSZ system is at least a combination of electronic and ionic mechanisms.

5. Conclusions

(1) MD modeling of atomic configuration with ~30,000 ions for a bi-crystal $\sum 5(310)/[001]$ grain boundary (GB) model resulted in the 8YSZ GB structure that agrees well with experimental observations.
(2) Diffusion coefficients of Y, Zr, and O ions in the 8YSZ system increase with the increase of the E-field and temperature. Though the temperature or thermal factor dominates the ionic diffusivities, E-field also plays a significant role. In particular, the bulk and GB diffusion coefficients increase by about one order of magnitude at a constant temperature as the E-field increases from 0V/cm to 1000V/cm.
(3) The formation of cation vacancies is more sensitive to the E-field than that of anion vacancies. Cation vacancy concentration increases obviously when an intense E-field (>~500-1000V/cm) is applied in the 8YSZ system, whereas the anion vacancy concentration does not change significantly with the variation of E-field.
(4) An intense E-field (≳500-1000V/cm) facilitates a certain amount of Zr ions to diffuse outside the GB region, leaving behind Zr vacancy-interstitial Frenkel defects concentrated in the vicinity of GBs, which contributes to the enhanced cation diffusivity during the flash sintering process.
(5) The reduction of electrostatic potential and GB space charge in the 8YSZ system at an intense E-field facilitates the increase of the disordering of the GB atomic structure and accelerates the O diffusivity at the GB region.
(6) An atomistic level mechanism of the non-thermal (E-field) contribution to the flash sintering of ionic ceramics is proposed in this work. An intense E-field promotes the formation of cation Frenkel pair defects, mainly at the GB region, enhancing the diffusivities of cations and anions in the 8YSZ system.

Declaration of Competing Interest

The authors declare that they have no known competing financial interests or personal relationships that could have appeared to influence the work reported in this paper.

Acknowledgments

This work was performed under the support of the US National Science Foundation (Award No. 1900876). The authors wish to thank the High-Performance Computing Cluster (HPCC) at SDSU for providing computing support for this project. WX thanks Dr. Alta Fang for helpful discussions on Poisson's equation. JJMM acknowledges financial support from the Junta de Extremadura through Grant IB16013 and from the Spanish Ministry of Economy and Competitiveness through Grant FIS2016-76359-P.

Supplementary materials

Supplementary material associated with this article can be found, in the online version, at doi:10.1016/j.actamat.2020.116596.

References

[1] E. Olevsky, D. Dudina, Field-Assisted Sintering: Science and Applications, Springer Nature IP, 2018.

[2] W. Chen, U. Anselmitamburini, J.E. Garay, J. Groza, Z. Munir, Fundamental investigations on the spark plasma sintering/synthesis processI. Effect of dc pulsing on reactivity, Mater. Sci. Eng. A 394 (2005) 132–138.
[3] O. Guillon, J. Gonzalez-Julian, B. Dargatz, T. Kessel, G. Schierning, J. Räthel, M. Herrmann, Field-assisted sintering technology/spark plasma sintering: mechanisms, materials, and technology developments, Adv. Eng. Mater. 16 (2014) 830–849.
[4] Z.A. Munir, U. Anselmi-Tamburini, M. Ohyanagi, The effect of electric field and pressure on the synthesis and consolidation of materials: a review of the spark plasma sintering method, J. Mater. Sci. 41 (2006) 763–777.
[5] U. Anselmi-Tamburini, J.E. Garay, Z.A. Munir, Fundamental investigations on the spark plasma sintering/synthesis process, Mater. Sci. Eng. A 407 (2005) 24–30.
[6] M. Yu, S. Grasso, R. Mckinnon, T. Saunders, M.J. Reece, Review of flash sintering: materials, mechanisms and modelling, Adv. Appl. Ceram. 116 (2017) 24–60.
[7] J.E. Garay, Current-activated, pressure-assisted densification of materials, Annu. Rev. Mater. Res. 40 (2010) 445–468.
[8] J. Luo, The scientific questions and technological opportunities of flash sintering: from a case study of ZnO to other ceramics, Scr. Mater. 146 (2018) 260–266.
[9] J.P. Kelly, O.A. Graeve, Spark plasma sintering as an approach to manufacture bulk materials: feasibility and cost savings, JOM 67 (2015) 29–33.
[10] T. Hungría, J. Galy, A. Castro, Spark plasma sintering as a useful technique to the nanostructuration of piezo-ferroelectric materials, Adv. Eng. Mater. 11 (2009) 615–631.
[11] J. Obare, W.D. Griffin, H. Conrad, Effects of heating rate and DC electric field during sintering on the grain size distribution in fully sintered tetragonal zirconia polycrystals stabilized with 3% molar yttria (3Y-TZP), J. Mater. Sci. 47 (2012) 5141–5147.
[12] R. Orrù, R. Licheri, A.M. Locci, A. Cincotti, G. Cao, Consolidation/synthesis of materials by electric current activated/assisted sintering, Mater. Sci. Eng. R. 63 (2009) 127–287.
[13] R. Castro, K. Van Benthem, Sintering: Mechanisms of Convention Nanodensification and Field Assisted Processes, Springer, 2013.
[14] J.T. Cahill, V.R. Vasquez, S.T. Misture, D. Edwards, O.A. Graeve, Effect of current on diffusivity in metal hexaborides: a spark plasma sintering study, ACS Appl. Mater. Interfaces 9 (2017) 37357–37363.
[15] K. Lu, Sintering of nanoceramics, Int. Mater. Rev. 53 (2008) 21–38.
[16] C. Wang, W. Ping, Q. Bai, H. Cui, R. Hensleigh, R. Wang, A.H. Brozena, Z. Xu, J. Dai, Y. Pei, C. Zheng, G. Pastel, J. Gao, X. Wang, H. Wang, J.-C. Zhao, B. Yang, X. (Rayne) Zheng, J. Luo, Y. Mo, B. Dunn, L. Hu, A general method to synthesize and sinter bulk ceramics in seconds, Science 368 (2020) 521–526.
[17] Z.A. Munir, D.V. Quach, M. Ohyanagi, Electric current activation of sintering: a review of the pulsed electric current sintering process, J. Am. Ceram. Soc. 94 (2011) 1–19.
[18] X. Song, X. Liu, J. Zhang, Neck formation and self-adjusting mechanism of neck growth of conducting powders in spark plasma sintering, J. Am. Ceram. Soc. 89 (2006) 494–500.
[19] M. Cologna, B. Rashkova, R. Raj, Flash sintering of nanograin zirconia in <5 s at 850°C, J. Am. Ceram. Soc. 93 (2010) 3556–3559.
[20] X.J. Chen, K.A. Khor, S.H. Chan, L.G. Yu, Preparation yttria-stabilized zirconia electrolyte by spark-plasma sintering, Mater. Sci. Eng. A 341 (2003) 43–48.
[21] Y. Bangchao, J. Jiawen, Z. Yican, Spark-plasma sintering the 8-mol% yttria-stabilized zirconia electrolyte, J. Mater. Sci. 39 (2004) 6863–6865.
[22] J. Stanley, C. Francis, A Study on the Phenomena of Flash Sintering with Tetragonal Zirconia, University of Colorado Boulder, 2013.
[23] R.K. Bordia, S.-J.L. Kang, E.A. Olevsky, Current understanding and future research directions at the onset of the next century of sintering science and technology, J. Am. Ceram. Soc. 38 (2017) 42–49.
[24] R. Raj, M. Cologna, J.S.C. Francis, Influence of externally imposed and internally generated electrical fields on grain growth, diffusional creep, sintering and related phenomena in ceramics, J. Am. Ceram. Soc. 94 (2011) 1941–1965.
[25] R.I. Todd, E. Zapata-Solvas, R.S. Bonilla, T. Sneddon, P.R. Wilshaw, Electrical characteristics of flash sintering: thermal runaway of Joule heating, J. Eur. Ceram. Soc. 35 (2015) 1865–1877.
[26] H. Majidi, K. Van Benthem, Consolidation of partially stabilized ZrO2 in the presence of a noncontacting electric field, Phys. Rev. Lett. 114 (2015).
[27] K.S. Naik, V.M. Sglavo, R. Raj, Flash sintering as a nucleation phenomenon and a model thereof, J. Eur. Ceram. Soc. 34 (2014) 4063–4067.
[28] R. Raj, Joule heating during flash-sintering, J. Eur. Ceram. Soc. 32 (2012) 2293–2301.
[29] J. Downs, Mechanisms of Flash Sintering in Cubic Zirconia, University of Trento, 2013.
[30] J. Narayan, A new mechanism for field-assisted processing and flash sintering of materials, Scr. Mater. 69 (2013) 107–111.
[31] E. Zapata-Solvas, S. Bonilla, P.R. Wilshaw, R.I. Todd, Preliminary investigation of flash sintering of SiC, J. Eur. Ceram. Soc. 33 (2013) 2811–2816.
[32] E.A. Olevsky, S.M. Rolfing, A.L. Maximenko, Flash (ultra-rapid) spark-plasma sintering of silicon carbide, Sci. Rep. 6 (2016) 33408.
[33] S. Grasso, Y. Sakka, N. Rendtorff, C. Hu, G. Maizza, H. Borodianska, O. Vasylkiv, Modeling of the temperature distribution of fla shsintered zirconia, J. Ceram. Soc. Jpn. 119 (2011) 144–146.
[34] E. Sortino, J.M. Lebrun, A. Sansone, R. Raj, Continuous flash sintering, J. Am. Ceram. Soc. 101 (2018) 1432–1440.
[35] W. Xu, K. Ramirez, S. Gomez, R. Lee, S. Hasan, A bimodal microstructure for fatigue resistant metals by molecular dynamics simulations, Comput. Mater. Sci. 160 (2019) 352–359.
[36] W. Xu, L.P. Dávila, Tensile nanomechanics and the Hall-Petch effect in nanocrystalline aluminium, Mater. Sci. Eng. A 710 (2018) 413–418.
[37] R.L. González-Romero, J.J. Meléndez, Yttrium segregation and oxygen diffusion along high-symmetry grain boundaries in YSZ, J. Alloys Compd. 622 (2015) 708–713.
[38] M. Kilo, M.A. Taylor, C. Argirusis, G. Borchardt, R.A. Jackson, O. Schulz, M. Martin, M. Weller, Modeling of cation diffusion in oxygen ion conductors using molecular dynamics, Solid State Ionics 175 (2004) 823–827.
[39] Y. Dong, L. Qi, J. Li, I.W. Chen, A computational study of yttria-stabilized zirconia: II. Cation diffusion, Acta Mater. 126 (2017) 438–450.
[40] W. Xu, A.P. Horsfield, D. Wearing, P.D. Lee, Classical and quantum calculations of the temperature dependence of the free energy of argon, Comput. Mater. Sci. 144 (2018) 36–41.
[41] W. Xu, X. Song, N. Lu, C. Huang, Thermodynamic and experimental study on phase stability in nanocrystalline alloys, Acta Mater. 58 (2010) 396–407.
[42] W.W. Xu, X.Y. Song, E.D. Li, J. Wei, J.X. Zhang, Thermodynamic study on phase stability in nanocrystalline Sm-Co alloy system, J. Appl. Phys. (2009) 105.
[43] W. Xu, A.P. Horsfield, D. Wearing, P.D. Lee, First-principles calculation of Mg/MgO interfacial free energies, J. Alloys Compd. 650 (2015) 228–238.
[44] R.L. González-Romero, J.J. Meléndez, D. Gómez-García, F.L. Cumbrera, A. Domínguez-Rodríguez, F. Wakai, Cation diffusion in yttria-zirconia by molecular dynamics, Solid State Ionics 204–205 (2011) 1–6.
[45] R.L. González-Romero, J.J. Meléndez, D. Gómez-García, F.L. Cumbrera, A. Domínguez-Rodríguez, Segregation to the grain boundaries in YSZ bicrystals: a molecular dynamics study, Solid State Ionics 237 (2013) 8–15.
[46] H.B. Lee, F.B. Prinz, W. Cai, Atomistic simulations of surface segregation of defects in solid oxide electrolytes, Acta Mater. 58 (2010) 2197–2206.
[47] J. Cheng, J. Luo, K. Yang, Aimsgb: an algorithm and open-source python library to generate periodic grain boundary structures, Comput. Mater. Sci. 155 (2018) 92–103.
[48] M. Jaipal, A. Chatterjee, Effect of the Σ5(310)/[001]tilt grain boundary on oxygen-ion movement in yttria-stabilized zirconia: insights from molecular dynamics, Acta Mater 165 (2019) 307–314.
[49] T. Oyama, M. Yoshiya, H. Matsubara, K. Matsunaga, Numerical analysis of solute segregation at Σ5 (310) [001]symmetric tilt grain boundaries in Y2O3-doped ZrO2, Phys. Rev. B - Condens. Matter Mater. Phys. 71 (2005).
[50] J. An, J.S. Park, A.L. Koh, H.B. Lee, H.J. Jung, J. Schoonman, R. Sinclair, T.M. Gur, F.B. Prinz, Atomic scale verification of oxide-ion vacancy distribution near a single grain boundary in YSZ, Sci. Rep. 3 (2013) 2680.
[51] S. Plimpton, LAMMPS-large-scale atomic/molecular massively parallel simulator, Sandia Natl. Lab. (2007).
[52] L. Vinet, A. Zhedanov, A "missing" family of classical orthogonal polynomials, J. Phys. A Math. Theor. (2011) 44.
[53] L. Wei-Zhong, C. Cong, Y. Jian, Molecular dynamics simulation of self-diffusion coefficient and its relation with temperature using simple Lennard-Jones potential, Heat Transf. Res. 37 (2008) 86–93.
[54] W. Callister, D. Rethwisch, Materials Science and Engineering: an Introduction, Wiley, 2007.
[55] V.V. Sizov, M.J. Lampinen, A. Laaksonen, Molecular dynamics simulation of oxygen diffusion in cubic yttria-stabilized zirconia: effects of temperature and composition, Solid State Ionics 266 (2014) 29–35.
[56] A. Stukowski, Visualization and analysis of atomistic simulation data with OVITO the Open Visualization Tool, Model. Simul. Mater. Sci. Eng. 18 (2010) 015012.
[57] A. Zangwill, Poisson's Equation, Mod. Electrodyn. (2019) 236–271.
[58] D. Gómez-García, J.J. Meléndez, R.L. González-Romero, A. Domínguez-Rodríguez, Segregation-induced grain boundary electrical potential in ionic oxide materials: a first principles model, Acta Mater. 58 (2010) 6404–6410.
[59] L. Zhang, A.V. Virkar, On space charge and spatial distribution of defects in yttria-stabilized zirconia, J. Electrochem. Soc. 164 (2017) F1506–F1523.
[60] B. Feng, N.R. Lugg, A. Kumamoto, Y. Ikuhara, N. Shibata, Direct observation of oxygen vacancy distribution across yttria-stabilized zirconia grain boundaries, ACS Nano 11 (2017) 11376–11382.
[61] M. Kilo, C. Argirusis, G. Borchardt, R.A. Jackson, Oxygen diffusion in yttria stabilised zirconia - experimental results and molecular dynamics calculations, Phys. Chem. Chem. Phys. 5 (2003) 2219–2224.
[62] R.A. De Souza, M.J. Pietrowski, U. Anselmi-Tamburini, S. Kim, Z.A. Munir, M. Martin, Oxygen diffusion in nanocrystalline yttria-stabilized zirconia: the effect of grain boundaries, Phys. Chem. Chem. Phys. 10 (2008) 2067–2072.
[63] Y. Dong, L. Qi, J. Li, I.W. Chen, A computational study of yttria-stabilized zirconia: I. Using crystal chemistry to search for the ground state on a glassy energy landscape, Acta Mater. 127 (2017) 73–84.
[64] M. Schie, S. Menzel, J. Robertson, R. Waser, R.A. De Souza, Field-enhanced route to generating anti-Frenkel pairs in HfO2, Phys. Rev. Mater. 2 (2018) 35002.
[65] J. Wang, H. Conrad, J. Luo, Interfacial engineering of solid electrolytes, J. Mater. 1 (2015) 22–32.
[66] X. Guo, Physical origin of the intrinsic grain-boundary resistivity of stabilized-zirconia: role of the space-charge layers, Solid State Ionics 81 (1995) 235–242.
[67] J.S.C.C. Francis, R. Raj, Flash-sinterforging of nanograin zirconia: field assisted sintering and superplasticity, J. Am. Ceram. Soc. 95 (2012) 138–146.
[68] K. Ren, J. Xia, Y. Wang, Grain growth kinetics of 3 mol. % yttria-stabilized zirconia during flash sintering, J. Eur. Ceram. Soc. 39 (2019) 1366–1373.

[69] R. Raj, M. Cologna, A. Prette, V. Sglavo, Methods of flash sintering, 13/562,040, 2013.
[70] M. Cologna, J.S.C. Francis, R. Raj, Field assisted and flash sintering of alumina and its relationship to conductivity and MgO-doping, J. Eur. Ceram. Soc. 31 (2011) 2827–2837.
[71] O. Fabrichnaya, F. Aldinger, Assessment of thermodynamic parameters in the system ZrO2-Y2O3-Al2O3, Zeitschrift Fuer Met. Res. Adv. Tech. 95 (2004) 27–39.
[72] Y.-M. Chiang, D.P. Birnie, W.D. Kingery, Physical Ceramics: Principles for Ceramic Science and Engineering, 1996.
[73] S.W. Kim, S.G. Kim, J. Il Jung, S.J.L. Kang, I.W. Chen, Enhanced grain boundary mobility in yttria-stabilized cubic zirconia under an electric current, J. Am. Ceram. Soc. 94 (2011) 4231–4238.